Aerodynamic Models for the Low Density Supersonic Decelerator (LDSD) Supersonic Flight Dynamics Test (SFDT)

John W. Van Norman[1]
Analytical Mechanics Associates, Hampton, Virginia, 23666

Artem Dyakonov[2], Mark Schoenenberger[3] and Jody Davis[4]
NASA Langley Research Center, Hampton, Virginia, 23681

Suman Muppidi[5]
ERC, Mountain View, California, 94040

Chun Tang[6] and Deepak Bose[7]
NASA Ames Research Center, Mountain View, California, 94035

Brandon Mobley[8]
Marshall Space Flight Center, Huntsville, Alabama, 35811

Ian Clark[9]
Jet Propulsion Laboratory, Pasadena, California, 91109

An overview of pre-flight aerodynamic models for the Low Density Supersonic Decelerator (LDSD) Supersonic Flight Dynamics Test (SFDT) campaign is presented, with comparisons to reconstructed flight data and discussion of model updates. The SFDT campaign objective is to test Supersonic Inflatable Aerodynamic Decelerator (SIAD) and large supersonic parachute technologies at high altitude Earth conditions relevant to entry, descent, and landing (EDL) at Mars. Nominal SIAD test conditions are attained by lifting a test vehicle (TV) to 36 km altitude with a large helium balloon, then accelerating the TV to Mach 4 and and 53 km altitude with a solid rocket motor. The first flight test (SFDT-1) delivered a 6 meter diameter robotic mission class decelerator (SIAD-R) to several seconds of flight on June 28, 2014, and was successful in demonstrating the SFDT flight system concept and SIAD-R. The trajectory was off-nominal, however, lofting to over 8 km higher than predicted in flight simulations. Comparisons between reconstructed flight data and aerodynamic models show that SIAD-R aerodynamic performance was in good agreement with pre-flight predictions. Similar comparisons of powered ascent phase aerodynamics show that the pre-flight model overpredicted TV pitch stability, leading to underprediction of trajectory peak altitude. Comparisons between pre-flight aerodynamic models and reconstructed flight data are shown, and changes to aerodynamic models using improved fidelity and knowledge gained from SFDT-1 are discussed.

---

[1] Senior Project Engineer, AIAA Member
[2] Aerospace Engineer, Atmospheric Flight and Entry Systems Branch, AIAA Member
[3] Aerospace Engineer, Atmospheric Flight and Entry Systems Branch, AIAA Member
[4] Aerospace Engineer, Atmospheric Flight and Entry Systems Branch, AIAA Member
[5] Research Scientist, AIAA Senior Member
[6] Research Scientist, AIAA Senior Member
[7] Aerospace Engineer, AIAA Associate Fellow
[8] Aerospace Engineer, AIAA Member
[9] LDSD Pricipal Investigator, AIAA Member

Nomenclature

A_{ref} = reference area
C = coefficient
C_A = axial force coefficient
C_{disp} = dispersed coefficient
CF = force coefficient
cg = center of gravity
C_l = rolling moment coefficient
CM = moment coefficient
C_m = pitching moment coefficient
C_{mq} = pitch damping coefficient
C_N = normal force coefficient
C_n = yawing moment coefficient
C_{nom} = nominal coefficient
C_{nr} = yaw damping coefficient
C_Y = side force coefficient
F = force
L_{ref} = reference length
M = moment
MRP = moment reference point
M_∞ = freestream Mach number
Re_d = Reynolds number w.r.t. diameter
T_∞ = freestream temperature
t = time
t/T = normalized time
u_1, u_2 = dispersion coefficients
u_{infl} = inflation rate coefficient
u_N = transient dispersion coefficient
V_∞ = freestream velocity
x, y, z = Cartesian components

Greek
α = angle of attack
α_T = total angle of attack
β = angle of sideslip
γ = ratio of specific heats
μ_∞ = freestream dynamic viscosity
ρ_∞ = freestream density
σ = standard deviation

Subscript
d = deployed
$disp$ = dispersed
nom = nominal
s = stowed
$trans$ = transient
x, y, z = Cartesian components

I. Introduction

EVERY successful mission to the surface of Mars has relied upon entry, descent, and landing (EDL) technologies derived from those developed in the 1960s and 70s for the Mars Viking program. While the successful 2012 landing of Mars Science Laboratory (MSL) demonstrated improvements in thermal protection systems (TPS), entry guidance, and propulsive terminal descent technologies, its aeroshell and supersonic parachute were traditional – and very near the size limit imposed by the launch vehicle payload shroud. Increased payload masses and access to higher landing altitudes require alternate decelerator technologies. To this end, concepts including supersonic retropropulsion[1] (SRP), hypersonic inflatable aerodynamic decelerators[2] (HIAD), and supersonic inflatable aerodynamic decelerators[3] (SIAD) are being developed and matured to enable high-mass Mars EDL operations.

The Low Density Supersonic Decelerator (LDSD) program is designed to mature SIADs and new supersonic parachutes for use in low density atmospheres such as that of Mars. LDSD technologies are demonstrated with a supersonic flight dynamics test (SFDT) campaign. The first flight test (SFDT-1) successfully delivered a 6 m diameter robotic mission class SIAD (SIAD-R) to test conditions and several seconds of flight on June 28, 2014. Additionally, a trailing ballute referred to as the parachute deployment device (PDD) was used to extract and deploy a large supersonic disksail (SSDS) parachute. Though the SFDT-1 trajectory and SSDS performance were off-nominal, the flight was a success in demonstrating the flight system concept and evaluating SIAD-R performance.

Prior to flight, SFDT-1 was simulated extensively with two flight simulation (FS) codes: Program to Optimize Simulated Trajectories II (POST2)[4] and Dynamics and Spacecraft Simulator for Entry, Descent and Surface Landing (DSENDS)[5]. The simulations were run in order to support vehicle development, conduct trade studies, and to target, evaluate, and optimize flight system performance. The focus of this paper is an overview of test vehicle (TV) aerodynamic models used in pre-flight simulations to target SFDT-1. Descriptions of the methodology used to generate each model and their implementation within the FS framework are presented. Comparisons are made between pre-flight predictions and aerodynamics reconstructed from SFDT-1 flight data, and post-flight improvements to models are discussed.

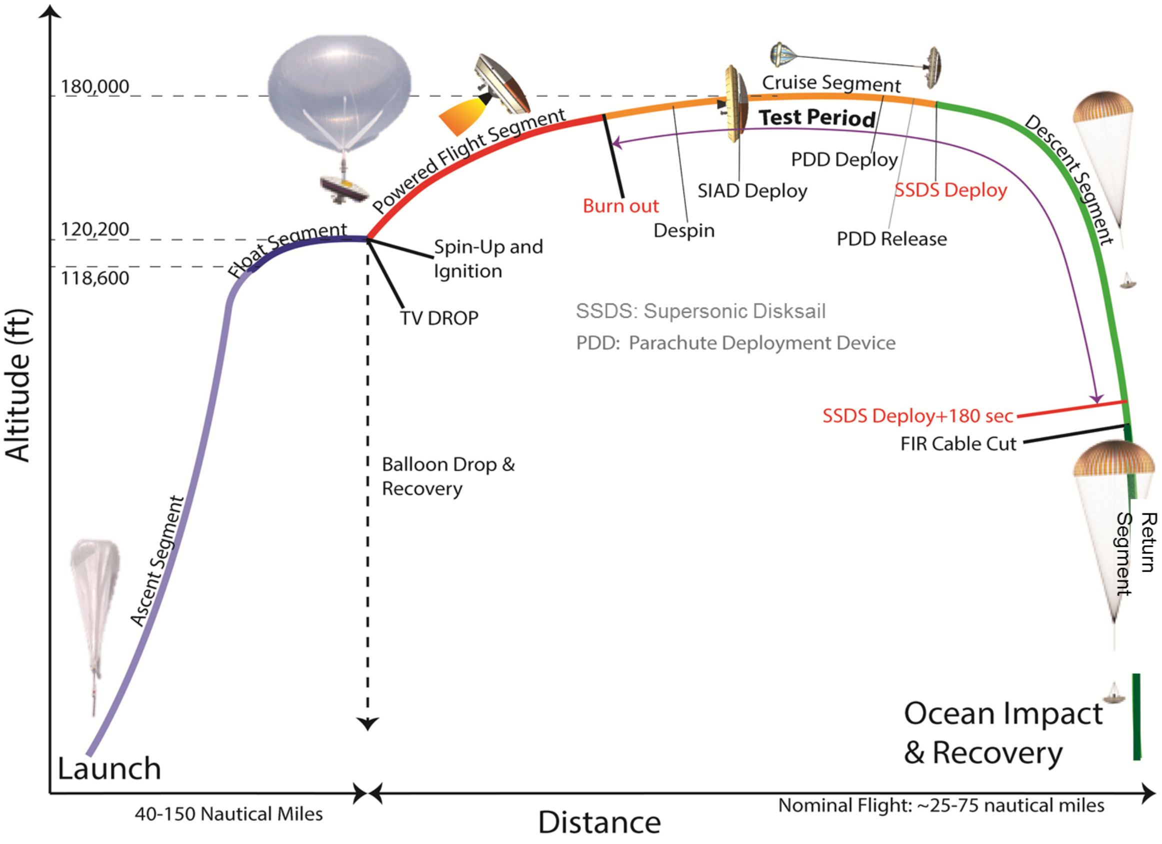

Figure 1. SFDT-1 concept of operations.

II. SFDT-1 Flight Operations and Test Vehicle

A. Flight Operations

LDSD flight operations, based at the Pacific Missile Range Facility (PMRF) on the Hawaiian island of Kauai, are similar to those of the Viking Balloon Launched Decelerator Test (BLDT) Program[6,7] conducted in 1972. Nominal SFDT flight begins with the inflation and deployment of a 34 million cubic foot helium balloon[8], which lifts the TV from a launch tower to a float altitude of approximately 36 km. The TV is suspended beneath the balloon at a hang angle which is targeted to produce a boost trajectory that will deliver the SIAD to its proper test conditions. Once desired balloon float conditions are met, the TV is released and spun up for gyroscopic stability. A boost motor is then ignited and accelerates the TV to Mach 4 and an altitude of approximately 53 km. After boost motor burnout, the TV is despun and the SIAD is deployed at a Mach number between 3.5 and 3.8. The TV is allowed to decelerate further before the PDD is deployed to extract the SSDS at about Mach 2.5, whereupon the PDD is jettisoned and the remainder of the flight system decelerates to eventual subsonic velocity and splashdown in the Pacific.

SFDT-1 was flown on June 28, 2014. The flight trajectory was off-nominal, lofting to an altitude of approximately 61 km. SIAD-R deployed successfully at Mach 4.08 and flew for nearly 80 s, followed by successful PDD deployment and SSDS extraction, however the parachute experienced structural failure during inflation. Nevertheless, stable powered flight, SIAD deployment and stability, and PDD operation were successfully demonstrated, and a wealth of flight data were obtained from a variety of onboard and ground-based measurements.

B. Test Vehicle

The SFDT-1 TV is a nonlifting blunt body configuration designed to deliver SIAD-R to supersonic test conditions which mimic those experienced during Mars entry. Detailed descriptions of the TV and its subsystems are documented in Ref. 8. With the SIAD stowed, the TV is a 4.7 m diameter axisymmetric aeroshell consisting of a spherical section forebody, conical aftbody, and an annular base plane surrounding a central aft-facing cavity. The 4.7 m diameter is a slight increase from the 4.5 m MSL aeroshell, and is the maximum size that can be accommodated for flight to Mars within an Atlas-V or Delta IV-H launch vehicle payload shroud[9]. The spherical section forebody is nearly identical to that of Orion, and possesses excellent drag performance, high volumetric efficiency, and avoids a phenomenon which induces a bounded static instability in the hypersonic flight of sphere-cones in the Martian atmosphere[10]. At its periphery, the forebody is joined to a rounded shoulder fairing, which doubles as a radome and meets the aftbody across a small aft-facing step. The conical aftbody is “wrapped” with the stowed, uninflated SIAD, which is held in place with a retention and restraint cover prior to its deployment. Numerous hardware elements are mounted to the base plane, including spin and despin motors and their plume deflectors, PDD and SSDS triple bridle assemblies, video cameras, and TPS blankets to protect sensitive components from spin, despin, and main motor plume environments. An Alliant Techsystems Inc. (ATK) STAR-

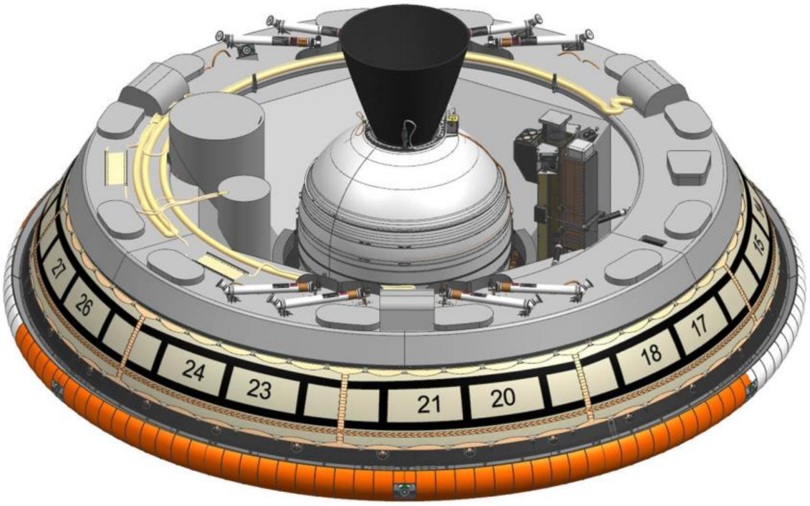

Figure 2. Isometric view, SFDT test vehicle aftbody with stowed SIAD-R. TPS blankets not shown.

48B long nozzle SRM, its propellant mass reduced to yield the SFDT trajectory profile, is centrally mounted within the base cavity, flanked by a video camera mast and cylindrical cans which house the PDD and SSDS.

With SIAD-R deployed, the TV total diameter nominally increases to 6 m. SIAD-R is an attached torus constructed from 27 circumferential gores of silicone-coated Kevlar fabric, and features a burble fence at its maximum diameter to ensure reliable flow separation and aerodynamic stability. SIAD deployment is accomplished with 9 pairs of gas generators, actuated sequentially in two pulses to first deploy and inflate the SIAD to shape, then to fully pressurize it. At its nominal fully inflated internal pressure of 28 kPa, the SIAD is essentially rigid at the upper bound 2.2 kPa dynamic pressure of flight, thus allowing for its modeling as a rigid body and making aerodynamic analysis straightforward with conventional numerical and ballistic range tools and methodology.

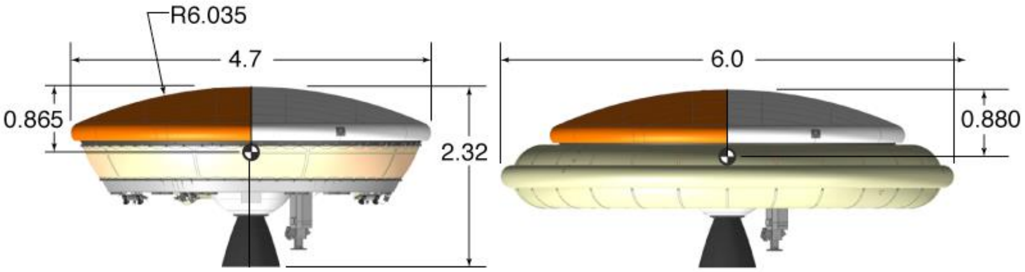

(a) (b)

Figure 3. SFDT test vehicle with stowed (a) and deployed (b) SIAD-R. Dimensions in meters.

III. Aerodynamic Models

TV aerodynamic models are integrated within the FS framework with a routine referred to as the aerodatabase (ADB). The ADB contains aerodynamic models for all phases of the TV flight: drop, spin-up, powered ascent, coast, despin, SIAD inflation, and SIAD cruise. The models are implemented within the ADB with tables of aerodynamic coefficients, aerodynamic uncertainties, spin and despin motor plume interaction models, a SIAD inflation model, and supporting subroutines including table look-up, interpolation, and blend routines which act in concert to link the aerodynamics of all SFDT flight simulation phases together. At each time step in a flight simulation, the FS code passes arguments to the ADB including Mach number, dynamic pressure, center of gravity (*cg*) location, angles of attack α and sideslip β, uncertainty dispersions, and state flags for motor operation and SIAD

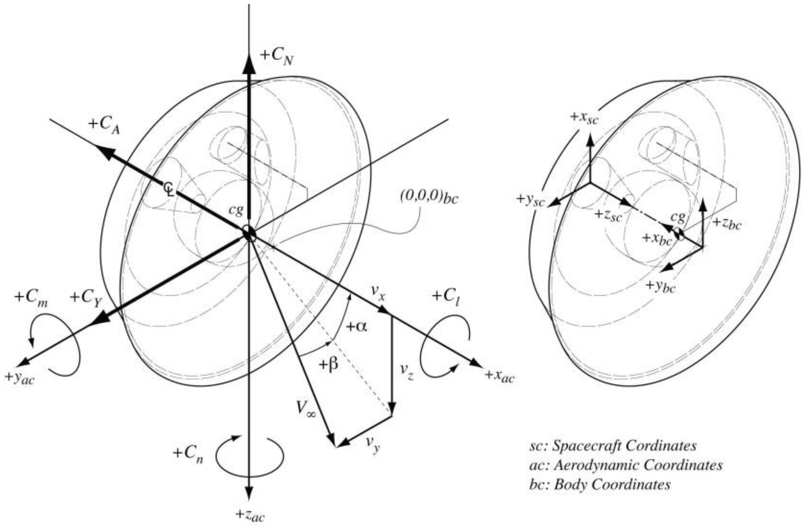

Figure 4. Coordinate system, aerodynamic angle, and aerodynamic coefficient conventions.

inflation. The ADB then interpolates aerodynamic coefficients from the appropriate tables, applies uncertainties and other models as required, and returns aerodynamic coefficients to the FS code.

TV aerodynamic models were constructed from computational and experimental data sources, where static aerodynamics were predicted with computational fluid dynamics (CFD) codes including the FUN3D[11], OVERFLOW[12], DPLR[13], and Loci-CHEM[14] flow solvers, and dynamic derivatives (i.e., pitch damping coefficients) for the TV in both stowed and deployed SIAD configurations were identified from ballistic range tests conducted in the Ames Research Center (ARC) Hypervelocity Free Flight Aerodynamics Facility (HFFAF)[15].

The ADB coordinate system, aerodynamic angle, and aerodynamic coefficient conventions are illustrated in Fig. 4. Moment coefficients tabulated within the ADB are expressed about the moment reference point (*MRP*), which is located on the axis of symmetry at the TV nose and is the origin of the body coordinate system (BCS). The BCS is referenced when passing *cg* location components to the ADB.

Aerodynamic uncertainty models within the ADB are formulated along the scheme used for MSL[16] as shown in Eq. 1. A dispersed coefficient C_{disp} is calculated from the nominal coefficient C_{nom} by applying an adder and multiplier, each perturbed independently with uncertainty dispersion coefficients u_1 and u_2 which range from -1 to 1 at the 3σ uncertainty limits.

$$C_{disp} = (C_{nom} + u_1 \cdot adder) \cdot (1 + u_2 \cdot multiplier) \qquad (1)$$

In a flight simulation, the dispersion coefficients are randomly generated with normal probability distributions and are held constant over the duration of the flight phase to which they apply. In FS Monte Carlo analysis, a new set of dispersion coefficients is generated for each run. Moment dispersions are applied at the *cg* so as to make them independent of moment transfer calculations.

Baseline uncertainties for the TV with deployed SIAD-R were chosen to be of the same magnitude as were used in the MSL ADB supersonic continuum regime uncertainty model. Adder and multiplier 3σ uncertainty limits for all SFDT-1 flight phases are tabulated in Table 1. Uncertainties for the powered phase are assigned in three distinct Mach regions, which allows for uncertainty sensitivity analyses partitioned by Mach number. Owing to the sensitivity of base drag to power-on effects, the powered phase C_A uncertainty model is split into forebody (f) and aftbody (a) contributions. The 3σ aftbody C_A uncertainty limits are equivalent to base pressure ranging from vacuum to freestream static, subject to an aftbody contribution upper limit C_A=5.

Flight phase		C_A	C_N, C_Y	C_m, C_n	C_{mq}, C_{nr}
Drop		±20%	±0.01, ±20%	±0.005, ±20%	n/a
powered	$M_\infty<0.25$	f: ±2% a: 0-min(5, $2/\gamma M^2$)	±0.01, ±20%	±0.005, ±20%	n/a
	$0.25\leq M_\infty\leq 1.5$	f: ±2% a: 0-min(5, $2/\gamma M^2$)	±0.01, ±20%	±0.005, ±20%	n/a
	$M_\infty>1.5$	f: ±2% a: 0-min(5, $2/\gamma M^2$)	±0.01, ±10%	±0.005, ±10%	n/a
Coast		±5%	±0.01, ±10%	±0.005, ±20%	±20%
SIAD-R		±10%	±0.01, ±10%	±0.005, ±20%	±20%

Table 1. Aerodynamic uncertainties for the SFDT test vehicle.

The following subsections describe the aerodynamic models for each TV flight phase, where references to event times correspond to those in nominal (undispersed) flight simulations.

A. Drop Phase

For aerodynamic modeling purposes, the nominal SFDT drop phase is defined as the interval which begins at the moment of balloon drop at *t*=0 s and ends at the moment of main motor ignition at *t*=2.15 s. During this period, the TV falls under the influence of gravity, and its total angle of attack is governed primarily by balloon hang angle and winds. The drop phase is characterized by short duration and low freestream dynamic pressure, which pre-flight simulations predicted not to exceed 3 Pa. Hence, freestream aerodynamic forces and moments imparted to the test vehicle are very small, as are resultant pitch rates. Consequently, no pitch damping model is implemented for the drop phase. Spin is imparted to the TV by rocket motors during the drop phase, and aerodynamic increments due to spin motor plume impingement are added to drop phase aerodynamics by way of a separate model described below.

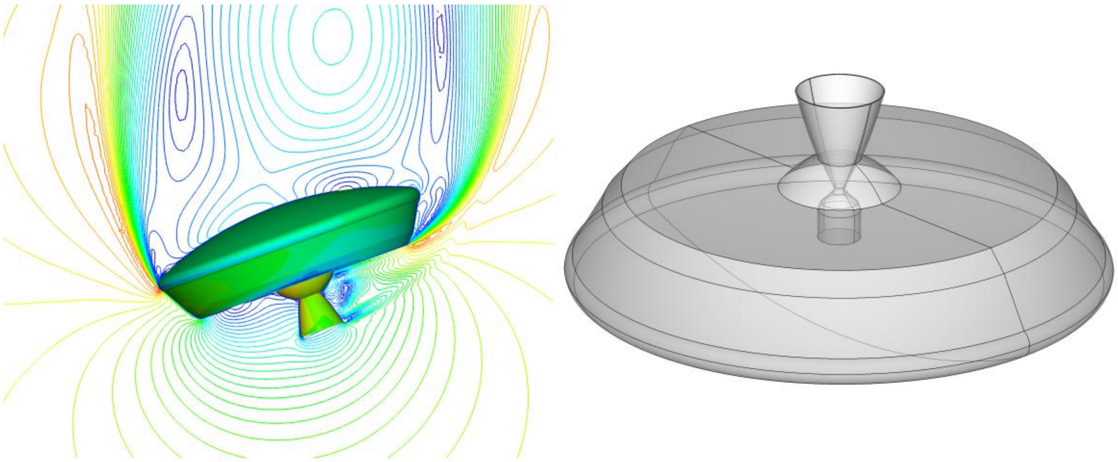

(a) (b)

Figure 5. a) Drop phase solution. b) Geometry used in drop, powered, and coast phase analyses.

Drop phase static aerodynamics were modeled from CFD simulations run with the FUN3D code, using a laminar flow model, nominal 36 km atmospheric conditions, and a Mach number of 0.266 over an angle of attack range from 0° to 180° in 10° increments. The computational domain was discretized with a fully tetrahedral computational mesh of approximately 9 million nodes generated with the Gridtool[17] and VGrid[18] codes. Characteristic far field boundary conditions were specified and TV surfaces were modeled as adiabatic viscous walls. The outer mold line (OML) was based on a notional shape developed before TV configuration was finalized, and lacked some features of the flight article including the aft-facing step, annular base cavity, and base plane protuberances.

Aerodynamic uncertainties during the drop phase were chosen to be greater than the MSL baseline, as the freestream Mach number approaches zero, and computations at those conditions were not attempted. Conservative analytical calculations and one-variable-at-a-time (OVAT) sensitivity studies conducted with POST2 indicated that SFDT flight performance is tolerant of order-of-magnitude errors in drop phase aerodynamic predictions.

B. Spin-Up

SFDT-1 spin-up nominally begins with the ignition of a pair of spin motors at t=0.36 s. They have a burn time of about 0.25 s, and are followed by ignition of a second pair of motors at t=1.66 s, also with a burn time of 0.25 s. The cumulative angular momentum imparted to the TV results in a nominal spin rate of 300°/s, which gives the TV gyroscopic stability during the powered ascent phase.

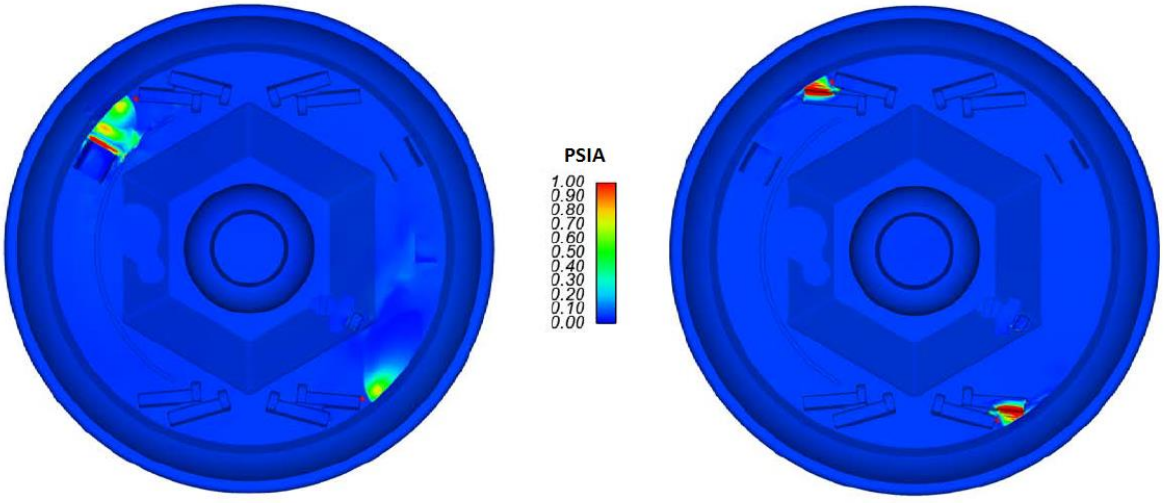

(a) (b)

Figure 6. Pre-flight model computed aftbody pressure contours for spin motors 1&3 (a) and 2&4 (b).

In many aerospace applications, plume flows generated by propulsive devices can impinge upon vehicle surfaces and/or interact with freestream flow, altering surface pressure distributions and producing unintended aerodynamic forces and moments[19,20]. The potential for such conditions arising as a consequence of spin motor operation was recognized as a possible source of rate and attitude error in early moments of SFDT flight which could result in an undesirable trajectory and failure to meet SIAD test conditions. CFD analyses were conducted to predict the extent of spin motor plume interaction and thus inform a model for use in flight simulations.

Pre-flight models of spin motor plume aerodynamic interactions were computed with a multi-code toolchain: the Reacting Multiphase Program (RAMP2)[21] and Boundary Layer Integral Matrix Procedure (BLIMPJ)[22] method-of-characteristics (MOC) codes, and the Loci-CHEM CFD code. The MOC codes were used to generate nozzle flow solutions, which in turn were used to prescribe nozzle boundary conditions for the Loci-CHEM simulations. Unstructured grids for Loci-CHEM were generated from CAD models using ANSA, SolidMesh, and AFLR3[23], and were highly detailed, with the final volume grids containing over 170 million cells. Viscous wall boundary conditions were used, with adiabatic nozzle surfaces and constant temperature (255 K) walls elsewhere. A frozen chemistry gas model was used with freestream air and surrogate exhaust gas species. The freestream was initialized with nominal 36 km atmospheric conditions at a Mach number of 0.05 and 0° angle of attack. A Reynolds-Averaged Navier-Stokes (RANS) scheme with SST turbulence model was used to compute the solutions, advanced second order in time until convergence to a steady flow state was attained. Plume-induced forces and moments were calculated by taking the difference between cases converged with and without the plume flows, neglecting spin motor thrust surfaces in all cases. Computed pressure contours on the backshell for each spin motor pair are shown in Fig. 4. Dimensional spin motor interaction forces and moments are tabulated in Table 2, where moments are expressed about the *MRP*.

motors	F_x	F_y	F_z	M_x	M_y	M_z
1 + 3	39.3	-260.4	308.9	-1098.9	160.4	692.5
2 + 4	508.5	25.2	-61.4	-1350.9	-80.8	-11.4

Table 2. Spin motor model plume induced forces (N) and moments (N*m) in aerodynamic coordinate system.

In the flight dynamic simulations, spin motor plume interaction models are activated by passing flags to the ADB during each motor pair burn. The interactions are calculated within the ADB from the entries in Table 2, which are converted to coefficient form using the instantaneous reference conditions. Resultant moment coefficients about the *cg* are then calculated, dispersed normally with a ±20% uncertainty at the 3σ uncertainty level, transferred back to the *MRP*, and added to the drop phase moment coefficients. Besides their use in calculating moment coefficient increments about the *cg*, force coefficient increments are neglected, as their effect on the TV trajectory is negligible.

Flight simulation results were extremely sensitive to the spin motor model, and predicted an altitude loss of 2.5 km at SIAD deployment due to impingement induced torques. The aftbody component layout used in the CFD analysis differed from the flight article due to interim configuration changes. A second analysis incorporating the flight geometry was undertaken but was not used to target SFDT-1 due to time constraints.

C. Powered Phase

The powered flight phase begins at the moment of STAR-48 ignition and ends at burnout, which for FS modeling purposes is defined as the moment when TV axial acceleration crosses zero. The production STAR-48B[24] is a SRM with an average thrust of 68.6 kN over a burn of 84.1 s, however the SFDT-1 flight motor propellant grain was offloaded by about 400 kg so as to reduce burn time to approximately 68 s and yield the desired trajectory. During a nominal powered phase, the TV gains approximately 17 km of altitude, its Mach number increases from about 0.04 to 4, and its total angle of attack decreases from 150° to about 2°. Over 1600 kg of propellant is burned from the offloaded motor, reducing the TV total mass by about half. The STAR-48 plume becomes increasingly underexpanded with increasing altitude, and nearly fills the wake region just prior to burnout.

The pre-flight powered phase aerodynamic model was constructed at trajectory points taken from an early flight simulation and tabulated in Table 3. A combination of Orion[25] aerodynamics and FUN3D solutions were used to populate the sub- and transonic solution space, and the OVERFLOW code was used to compute trans- and supersonic regime solutions. At the overlap Mach number of 0.91, aerodynamics were averaged between results from the two codes. In addition to the powered solutions, power-off solutions were computed at all points for use in other flight phase models. For lack of supporting data, a pitch damping model was not implemented for the powered phase.

M_∞	V_∞ (m/s)	ρ_∞ (kg/m^3)	T_∞ (K)	μ_∞ (N·s/m^2)	Re_d	α_T
0.266	82.6	6.664E-03	239.4	1.544E-05	1.676E+05	0°-180°
0.505	156.9	6.293E-03	240.4	1.549E-05	2.996E+05	0°-60°
0.905	283.2	5.190E-03	245.5	1.576E-05	4.384E+05	0°-40°
1.507	478.0	3.480E-03	253.0	1.614E-05	4.844E+05	0°-30°
2.486	800.7	2.199E-03	262.0	1.660E-05	4.985E+05	0°-20°
4.037	1309.3	1.466E-03	269.8	1.700E-05	5.306E+05	0°-20°

Table 3. Flow conditions for powered phase aerodynamic model.

All pre-flight powered phase aerodynamic computations analyzed the same simplified axisymmetric OML as was used for drop phase computations, which omitted the base cavity and other geometric features of the flight article. TV spin was not modeled in the simulations. Surface grids were configured with separate domains for fore- and aftbody regions so that their aerodynamic contributions and uncertainties could be independently accounted for and dispersed. Convergent-divergent nozzle flows were computed for all powered cases, using subsonic total pressure, total temperature inflow boundary conditions applied to a plane upstream of a convergent plenum. At the time of analysis, flight motor properties were not fully known, so nominal thrust and chamber pressure were assumed to take average values during the burn, held constant at all trajectory points. In calculating the powered phase aerodynamics, thrust surfaces are omitted from the force and moment summation so as to isolate the aerodynamics from thrust. The STAR-48 thrust model used in flight simulations resides in the FS codes and is not used in any way by the ADB.

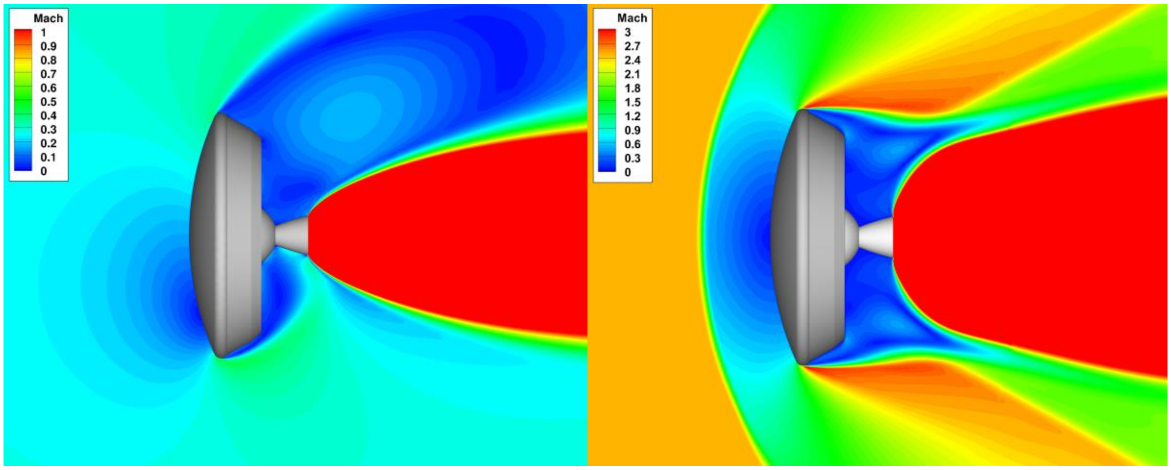

(a) (b)

Figure 7. Powered phase solution Mach contours: a) Mach 0.266, α=30°; and b) Mach 2.486, α=0°

FUN3D sub- and transonic powered phase solutions were computed on fully tetrahedral grids of about 9 million nodes using a Roe flux scheme, Menter-SST turbulence model, Van Leer flux limiter, no-slip adiabatic walls, and a calorically perfect, single species gas model with γ=1.4. Nozzle inflow total temperature was set to 3520 K and the total pressure was adjusted to yield 66 kN thrust. In order to avoid solution divergence at the inflow boundary condition, the computational procedure required several restarts, each with an increase in total inflow conditions until the desired thrust was obtained. The solution was then advanced with a global time step until a steady aerodynamic solution was obtained, or in the case of an unsteady solution, advanced over a sufficient number of iterations to capture the mean aerodynamics. At the Mach 0.266 condition, the nozzle flow entrained the freestream such that velocity and angle of attack were influenced upstream to a distance which increased with simulation time. This feature reduced confidence in the solutions, so aerodynamics for this Mach number were taken from Orion data and adjusted with an axial force coefficient increment ΔC_A=0.91 taken from the computations at zero angle of attack.

OVERFLOW trans- and supersonic regime solutions were computed on an overset grid system of about 20 million points using a central differencing scheme, Baldwin-Barth turbulence model, no-slip adiabatic walls, and a two-species gas model with freestream γ=1.4. A nominal chamber pressure of 568 psia and exit exhaust gas γ=1.21 were assumed, the latter based on properties of aluminized ammonium perchlorate-HTPB propellant. The nozzle inflow boundary condition was thus specified, with a resultant net thrust of 58 kN. The computational procedure required several restarts, incrementally increasing nozzle inflow pressure and temperature in order to avoid solution divergence. Computations were advanced with a local timestepping scheme until aerodynamics were converged to a steady state.

Plume-induced effects observed in the powered phase solutions included increases in axial force and pitch stiffness. As the STAR-48 plume entrains the TV wake flow, it reduces the base pressure by aspiration[26] and thus increases drag. As shown in Fig. 8, the base flow scavenging effect becomes biased to the windside at angle of attack, further reducing pressure there and strengthening the pitching moment in comparison to the case with no plume. Consequently, the TV has a tendency to turn into the wind more readily when the motor is firing. Plume flow effects are strongest in the sub- to transonic regime, and become insignificant with increasing Mach number as the TV total angle of attack decreases and aerodynamics become dominated by the forebody flow.

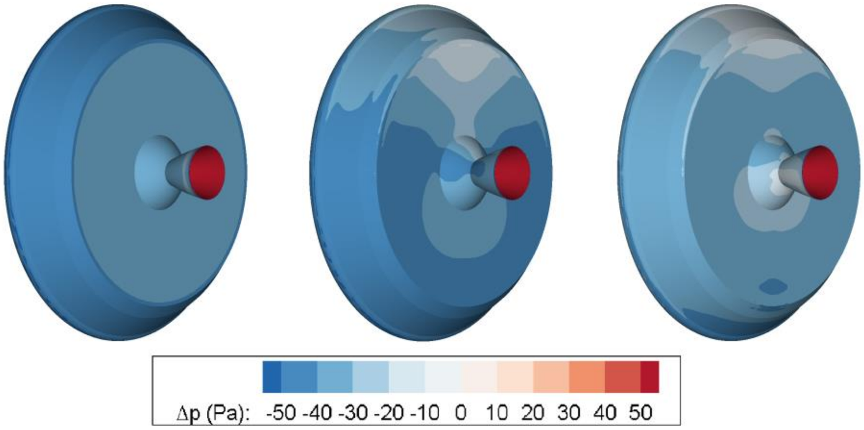

Figure 8. Power-on base pressure effects: Mach 0.505 at 0°, 10°, and 20° angle of attack.

In flight simulations, the transition from powered phase to coast phase aerodynamics and uncertainties at the end of the STAR-48 burn is effected over an interval of 0.25 s which begins at the moment of burnout. During this interval, the FS code passes a dimensionless transition time t to the ADB which ranges from 0 to 1, and is used to blend aerodynamic coefficients and uncertainties along S-curves calculated by Eq. 2.

$$C = C_{powered} + (C_{coast} - C_{powered})(1 - (1 + \cos(\pi t))/2) \qquad (2)$$

D. Coast

The coast phase is defined as the time between STAR-48 burnout and the onset of SIAD inflation. Coast nominally begins at about Mach 4 and lasts for approximately 6 s. Despin occurs during the coast phase and is treated with a despin motor plume interaction model described below. Coast phase static aerodynamics were taken from power-off OVERFLOW and FUN3D solutions. Additional supersonic high-alpha solutions were computed for the derivation of tumbling TV drag in off-nominal scenarios. The coast phase pitch damping model was derived from ballistic range data compiled over 12 shots at Mach numbers from 3.16 to 3.67.

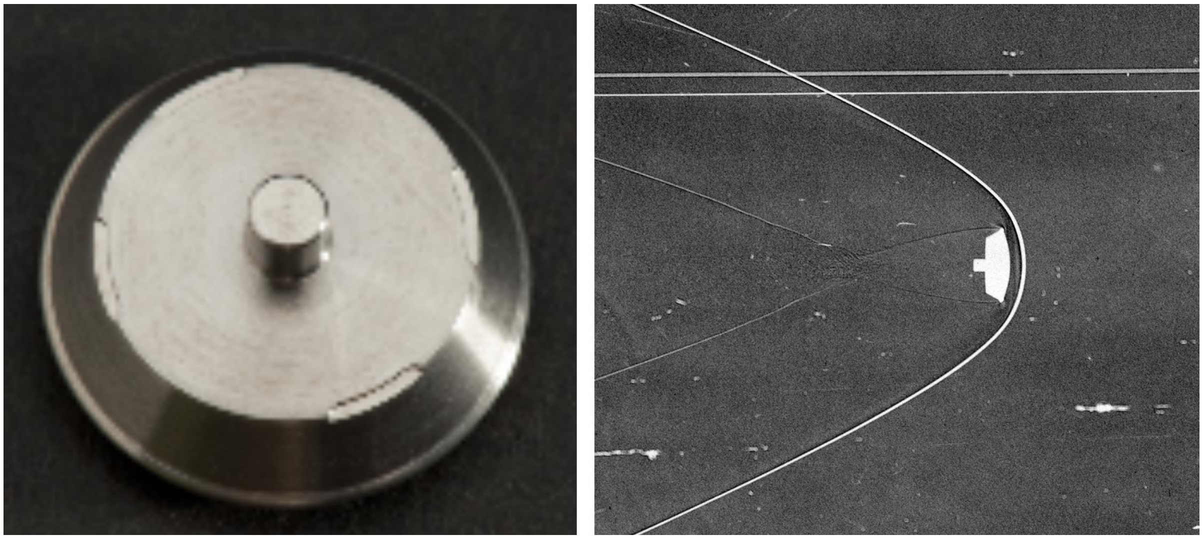

(a) (b)

Figure 9. a) Coast phase ballistic range model, and b) shadowgraph from Mach 3.15 shot.

E. Despin

Despin occurs during the coast phase and nominally reduces the TV roll rate to zero by action of two pairs of despin motors. Despin motor plume interactions were computed with the Loci-CHEM CFD code in much the same manner as the spin motor interactions, but with the despin motor geometry and at different freestream conditions. Despin flowfield solutions were generated for the TV with a 342°/s roll rate, at zero angle of attack and Mach 4.24 in a 50 km atmosphere. Despin model implementation is identical to that of the spin-up model, though with a larger 3σ uncertainty of ±40% distributed normally. The larger uncertainty is intended to reflect the greater dynamic pressure and thus potential for interaction with the freestream at despin conditions, in addition to angle of attack variability in the flight simulations. Predicted despin motor plume-induced forces and moments are tabulated in Table 4, where moments are expressed about the *MRP*. In flight simulations, TV dynamics had low sensitivity to the despin plume model interactions.

motors	F_x	F_y	F_z	M_x	M_y	M_z
5 + 7	3731.5	16.0	-1.1	603.9	-4.5	-8.1
6 + 8	3461.8	169.4	224.2	762.9	252.6	-341.1

Table 4. Despin motor model plume induced forces (N) and moments (N*m) in aerodynamic coordinate system.

F. SIAD Inflation

For modeling purposes, the SIAD inflation phase is defined as the event that begins at the onset of SIAD deployment and ends when the SIAD has reached its design shape and internal pressure. At nominal test conditions, full SIAD-R inflation occurs in about 0.4 s.

The pre-flight SIAD-R inflation model is based upon results published by Bohon and Miserentino[27], who conducted wind tunnel experiments with attached inflatable decelerators. The inflation model consists of two primary components: a transition from stowed to deployed SIAD aerodynamics, and a transient disturbance arising from asymmetric SIAD deployment.

The aerodynamic transition between stowed and fully deployed SIAD states follows an S-curve which in principle follows the change in overall vehicle shape and size. This transition is modeled over the inflation time T during which the position within the interval t/T is passed from the FS code to the ADB. In the flight dynamic simulations, A_{ref} and L_{ref} are changed to deployed SIAD values at the beginning of SIAD inflation, and aerodynamic force and moment coefficients are blended using Eqs. (3) and (4), where subscripts s and d correspond to stowed and deployed SIAD, respectively. The inflation rate coefficient u_{infl} is dispersed normally over ±1 and changes the shape of the inflation blend curve. The dimensionless blend fraction is plotted with its ±3σ dispersions in Fig. 11.

$$CF = \frac{(CF \cdot A_{ref})_s}{(A_{ref})_d} + \left[CF_d - \frac{(CF \cdot A_{ref})_s}{(A_{ref})_d} \right] \left(1 - \left(\frac{1+\cos[2\pi(t/T)]}{2} \right)^{1+0.3u_{infl}} \right) \tag{3}$$

$$CM = \frac{(CM \cdot A_{ref} \cdot L_{ref})_s}{(A_{ref} \cdot L_{ref})_d} + \left[Cm_d - \frac{(CM \cdot A_{ref} \cdot L_{ref})_s}{(A_{ref} \cdot L_{ref})_d} \right] \left(1 - \left(\frac{1+\cos[2\pi(t/T)]}{2} \right)^{1+0.3u_{infl}} \right) \tag{4}$$

The transient disturbance model is also based upon data from Ref. 27, in which a substantial transient normal force coefficient (C_N=0.2) was recorded during inflation with the SIAD at zero angle of attack. The model assumes a normal force disturbance applied in a random radial direction and a correlated moment equivalent to “blanking” a 40° sector of the SIAD, intended to simulate failure of a pair of gas generators. The disturbance takes the shape of a wave, and its magnitude is dispersible from 0-100% via coefficient u_N with a uniform probability distribution. Transient normal force and moment coefficients are modeled with Eqs. (5) and (6), and the undispersed time-varying normal force coefficient is plotted in Fig. 11.

$$C_{N,trans} = 0.2 \cdot u_N \left(\frac{1-\cos\left[2\pi(t/T)^{0.3}\right]}{2} \right)^8 \tag{5}$$

$$C_{m,trans} = 0.191 \cdot C_{N,trans} \tag{6}$$

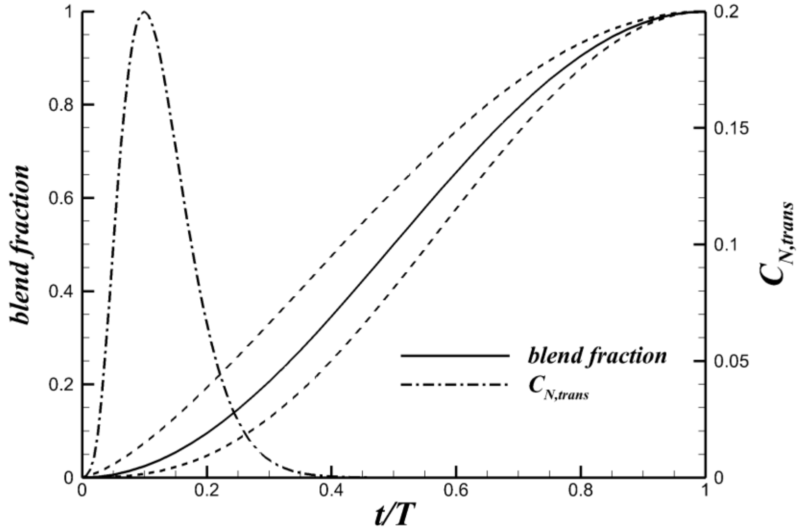

Figure 11. SIAD inflation and transient disturbance model curves.

G. SIAD-R Cruise Phase

The SIAD-R cruise phase begins at full inflation and continues until SSDS deployment. At the nominal ratio of internal pressure to freestream dynamic pressure, the fully inflated SIAD-R behaves much like a rigid body, as demonstrated in rocket sled testing[28] where peak measured deformations were on the order of 30 mm. This aspect of SIAD-R makes it relatively simple to analyze in comparison to larger, ram-air inflated isotensoids which require deformed OML analysis[29].

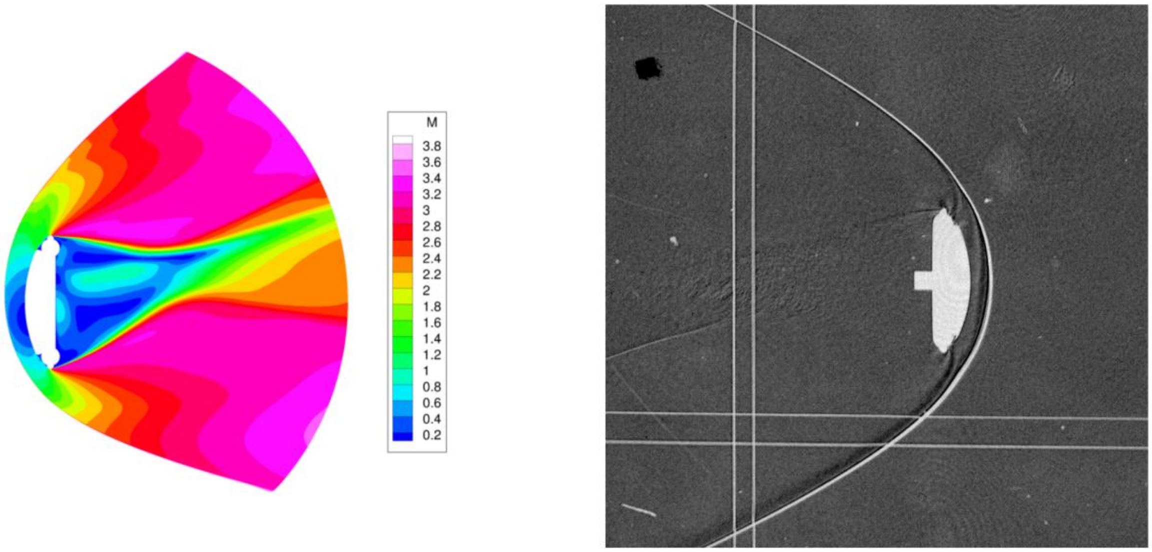

(a) (b)

Figure 12. SIAD cruise: a) computed Mach contours and (b) ballistic range shadowgraph.

As detailed in Ref. 30, SIAD-R cruise static aerodynamics were modeled from CFD simulations run with the DPLR code, using the Menter-SST turbulence model for nominal flight conditions at Mach 3.97, 3.0, and 2.12. Solutions were computed at angles of attack from 0° to 30° with 10° increment for the Mach 3.97 condition, and from 0° to 90° in 15° increment for the other Mach numbers. Four OMLs were analyzed, including two idealized axisymmetric geometries: one with a flat base and one with the STAR-48 nozzle; and two as-measured geometries taken from laser scans of the inflated SIAD-R, gridded to resolve individual SIAD gores and determine the effect of the geometry on aerodynamics and aeroheating. All geometries omitted the base cavity and protuberances. Hyperbolic grids of the idealized flat base and nozzle-included geometries contained about 10 million and 13 million points, respectively, while the laser scan grids were larger to capture geometric detail and contained about 59 million points. Aerodynamic variance due to differences between OMLs was within 3%. Solutions exhibited unsteady flow features due to separation and reattachment at the aeroshell-SIAD interface and burble region, and massive wake flow separation. Aerodynamic variances due to flow unsteadiness were about 1% of the means.

The SIAD-R cruise phase pitch damping model was derived from ballistic range test results compiled from 37 shots at Mach numbers from 2.03 to 3.85.

IV. Comparison of Pre-Flight Predictions to Reconstructed Flight Data

SFDT-1 flight data were collected from a variety of sources for use in flight reconstruction, including meteorological balloons and sounding rockets, on-board inertial measurement unit (IMU) and global positioning system (GPS), and ground-based tracking radars. With atmospheric properties reconstructed from meteorological measurements, the remainder of the data were combined with thrust and mass models to reconstruct the trajectory and aerodynamics using NewSTEP[31]. NewSTEP is an Iterative Extended Kalman Filter (IEKF) code that has seen use in reconstruction activities for many noteworthy flight projects, including Hyper-X, Ares I-X, and MSL[32-34].

The powered phase presented a particular challenge to the aerodynamic reconstruction effort. A chamber pressure transducer intended for use in the STAR-48 thrust reconstruction was not flown due to an electrical malfunction. With the flight thrust profile unknown, errors in the pre-flight thrust and aerodynamic axial force models could not be separated. In the final reconstruction, adjustments were made to the thrust model such that combined thrust and axial force would yield the reconstructed axial accelerations.

Aerodynamic predictions are compared against reconstructed aerodynamics in the following sections, where the pre-flight production ADB (version 1.3.4) is called at reconstructed flight conditions at each time step. Reconstructed data are from NewSTEP SFDT-1 run 5.5 and are interpolated to 100 Hz. For brevity, ADB refers to pre-flight aerodynamic models, and BET (best estimated trajectory) refers to reconstructed quantities. It should be noted that the reconstructed aerodynamics are based on measured accelerations and rates, where contributions from spin, despin, and boost motors are not separated from those due to aerodynamics.

A. Drop and Spin-Up Phase

The drop and spin-up phase BET axial force and total angle of attack plotted in Fig. 13(a) show results which suggest a limitation of the reconstruction method. Under- and overshoots seen at the edges of balloon drop and spin motor events appear to be filtering artifacts. At *t*=0, the BET total angle of attack and axial force are 54.4° and -14.6 kN, respectively, in disagreement with the assumption that flow incident to the forebody will yield a positive axial force. Similar unlikely combinations are seen before the first and second spin motor firings, where flow is incident to the aftbody and reconstructed axial forces are positive.

Assuming equal spin motor thrusts and symmetric thrust vector alignments, the spin-up model is assessed by subtracting ADB drop phase pitch and yaw moments from the respective BET moments, then comparing the remainder to spin model moments resolved about the *cg*. The comparison is made for the first spin motor pair, which is predicted to produce the larger pitch and yaw interactions. As plotted in in Fig. 13(b), the comparison indicates that the model does not correctly predict the sign of the reconstructed yaw interaction. The reconstructed interaction magnitudes cannot be clearly defined, however, due to numerical oscillations in the reconstructed solution.

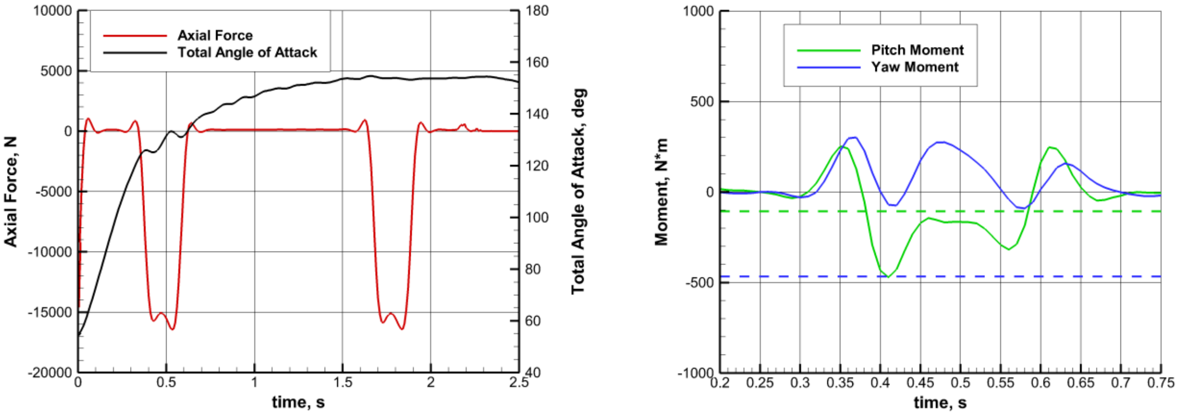

(a) (b)

Figure 13. a) Reconstructed drop phase axial force and total angle of attack, and b) spin-up interaction pitch and yaw moments, where dashed lines denote model pitch and yaw moment values.

B. Powered Phase

During the powered phase, the reconstructed side and normal force data are extremely noisy and difficult to interpret, particularly in the first several seconds, so we restrict our analysis to the period $t \geq 10$ s. After significant data smoothing, BET side and normal force coefficients are plotted in Fig. 14(a). Bias is apparent in both reconstructed coefficients, which should oscillate about zero while the TV is spinning due to axisymmetric aerodynamics. The bias is seen to persist over the duration of the burn, and suggests a thrust misalignment, radial *cg* offset, or combination of the two. In Fig. 14(b), the BET moment coefficients are plotted and biases are seen in these coefficients as well, however they do not persist strongly as is the case with the forces normal to the spin axis.

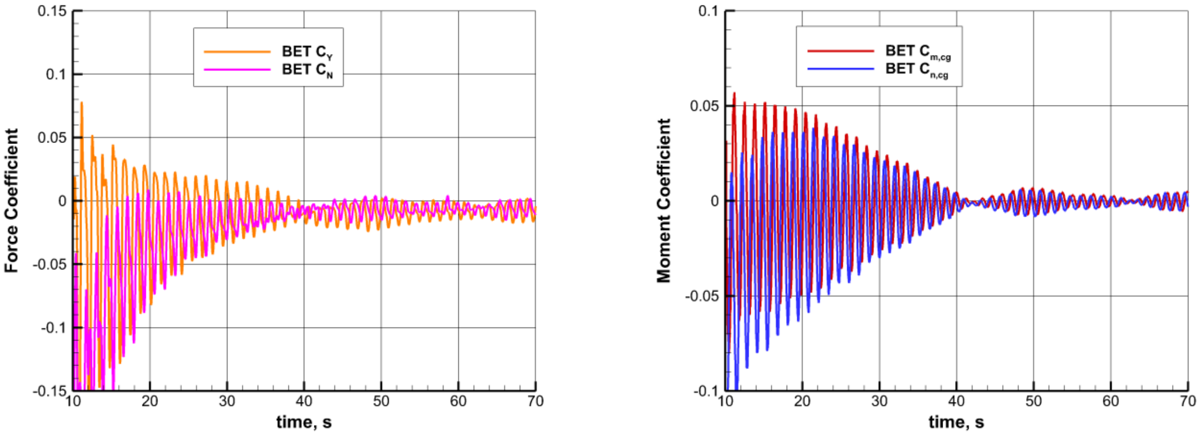

(a) (b)

Figure 14. Reconstructed a) side and normal force coefficients, and b) pitch and yaw moment coefficients.

Reconstructed angles of attack and sideslip plotted in Fig. 15(a) are symmetric. Combined with a lack of persistent bias in moment coefficients, this feature may indicate a thrust misalignment which counters the effect of a radial *cg* offset. The mean total normal force is nearly constant and its correlation to total angle of attack is weak, as shown in Fig. 15(b). Because the normal force signal contains a great deal of noise and is modified by data smoothing, a definitive cause for the bias is unidentifiable, however it is likely a combination of small radial *cg* offset and small thrust misalignment angle.

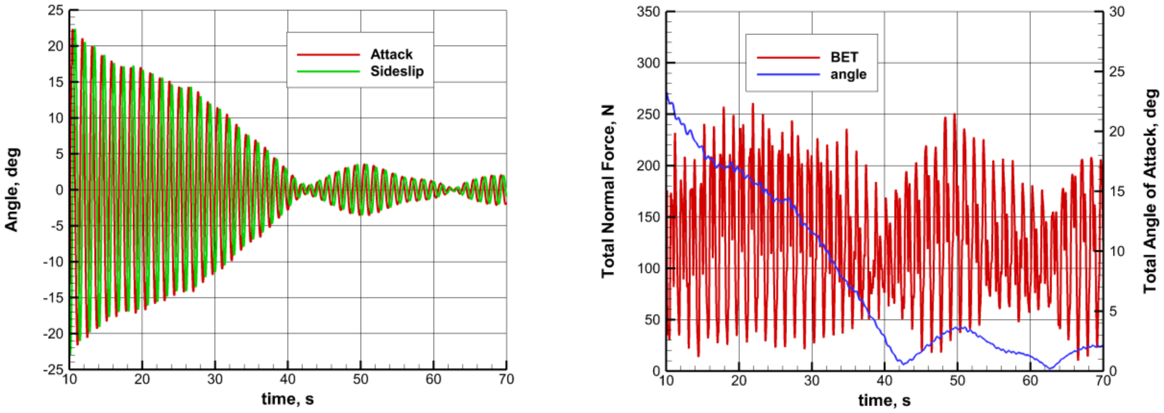

(a) (b)

Figure 15. a) BET angles of attack and sideslip, and b) total normal force and angle of attack.

A comparison of BET and ADB total moment coefficient plotted in Fig. 16(a) shows that the powered phase model moment coefficient was overpredicted. The overpredicted moment causes the TV to point more readily into the freestream velocity vector while at large angle of attack, resulting in reduced flight path angle. In simulation, this overpredicted pitch stability leads to trajectories with underpredicted peak altitude. Post-flight analyses indicated that the overpredicted moment coefficient was a significant aerodynamic contributor to SFDT-1 lofting[35].

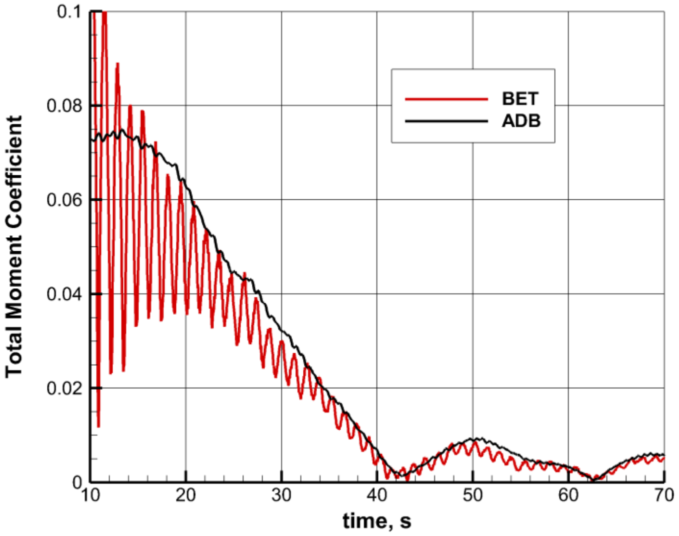

Figure 16. Total moment coefficients.

C. Coast

According to reconstruction, the SFDT-1 coast phase took place over the interval $73.0 \le t \le 82.5$ s, during which time the Mach number decreased from 4.29 to 4.09, the dynamic pressure decreased from 556 Pa to 333 Pa, and the TV total angle of attack ranged from 0.18° to 3.05°. Over this range of conditions, the ADB queries a single table corresponding to OVERFLOW solutions run at Mach 4.04. As plotted in Fig. 17(a), the reconstructed axial force coefficient changes by 4.2% over the interval and at maximum exceeds the prediction by about 3.3%, or a 2σ uncertainty. The normal force is in good agreement with predictions as shown in Fig. 17(b).

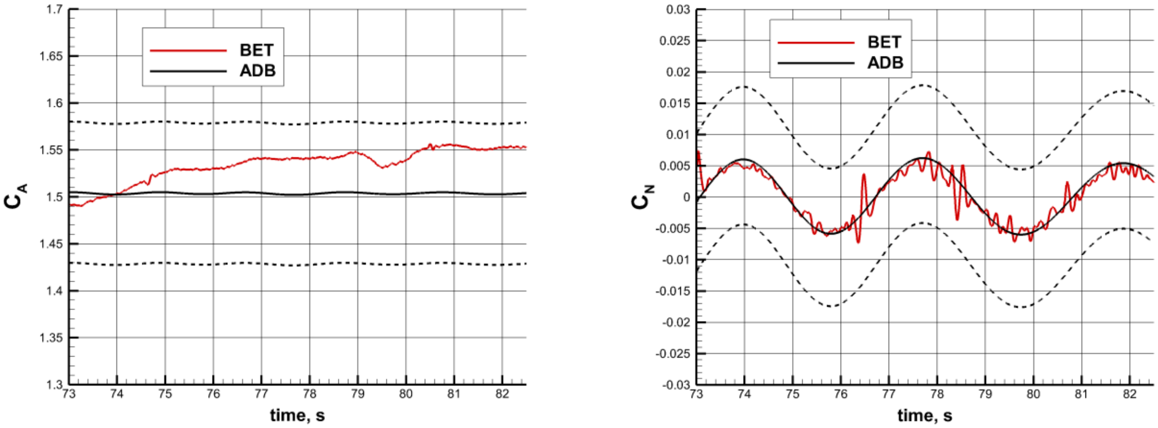

(a) (b)

Figure 17. a) Axial force and b) normal force coefficients, dashed lines denote model 3σ uncertainties.

The pitching moment coefficient is also in excellent agreement with predictions as shown in Fig. 18(a). A bias in the reconstructed yawing moment is correlated to a nonzero sideslip trim angle shown in Fig. 18(b). The mean angle of sideslip is approximately -0.5° and could be the result of a radial *cg* offset about -0.0035 m along the y-axis.

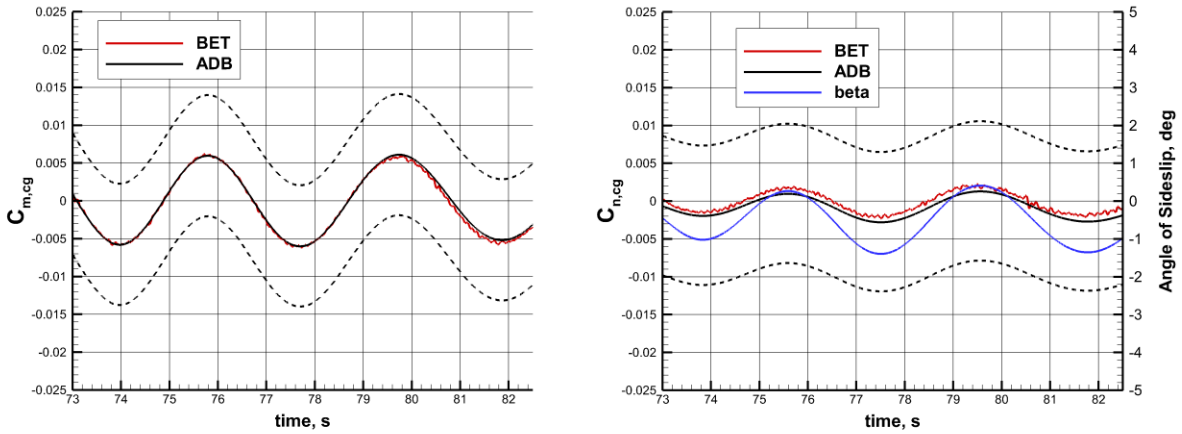

(a) (b)

Figure 18. a) Pitching moment coefficients and b) yawing moment coefficients with nonzero sideslip trim angle. Dashed lines denote model 3σ uncertainties.

D. Despin

Flight reconstruction indicates that despin motor firings occured at approximately *t*=72.05 s and *t*=72.55 s, where motors 6 & 8 are fired before motors 5 & 7. Similar to the spin motor result, the reconstructed despin motor axial force disturbance shows evidence of numerical oscillation as shown in Fig. 19(a). The despin model predicted a substantial yaw moment interaction for the first motor pair, and negligible interactions for the second pair. The predicted yaw moment is denoted by the dashed line in Fig. 19(b). In this case, it appears that numerical under- and overshoots are swamping the desired signal. Analysis of measured accelerations is probably required to obtain an accurate reconstruction of the despin motor interaction and is beyond the scope of the current work.

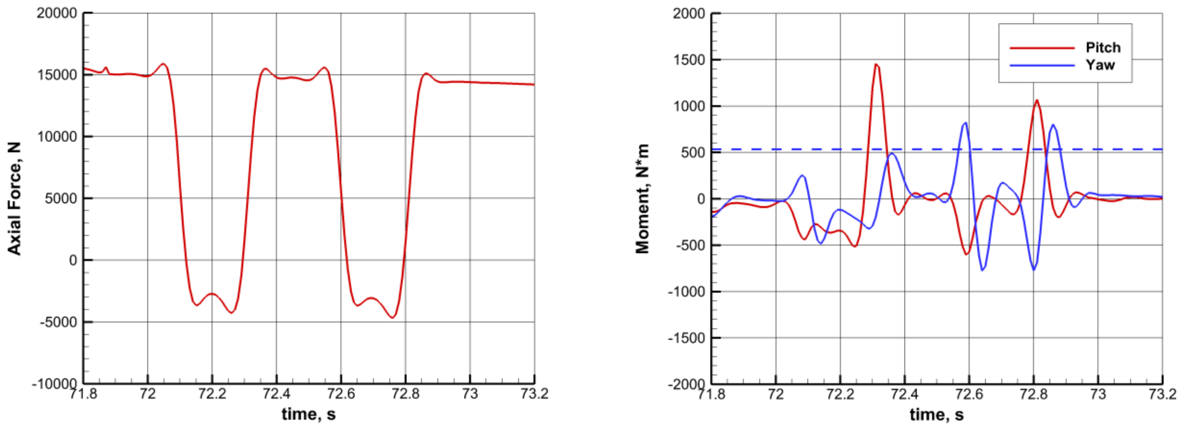

(a) (b)

Figure 19. Despin a) axial force disturbance, and b) interaction pitch and yaw moments, where the dashed line denotes the predicted yaw moment.

E. SIAD Inflation

The reconstructed axial force trace plotted in Fig. 20(a) indicates that the SIAD-R inflation began at approximately *t*=82.6 s. The reconstruction here obviously suffers from the same under- and overshoots seen in other transient events, e.g., drop, spin, and despin, as there is no aerodynamic explanation for the oscillatory behavior. We conclude that the method of reconstruction is not amenable to transient events, and so rather look to the aerodynamic angle history to assess the inflation model. In Fig. 20(b), reconstructed angles of attack and sideslip are plotted, and no appreciable disturbance in vehicle dynamics are apparent in their time histories.

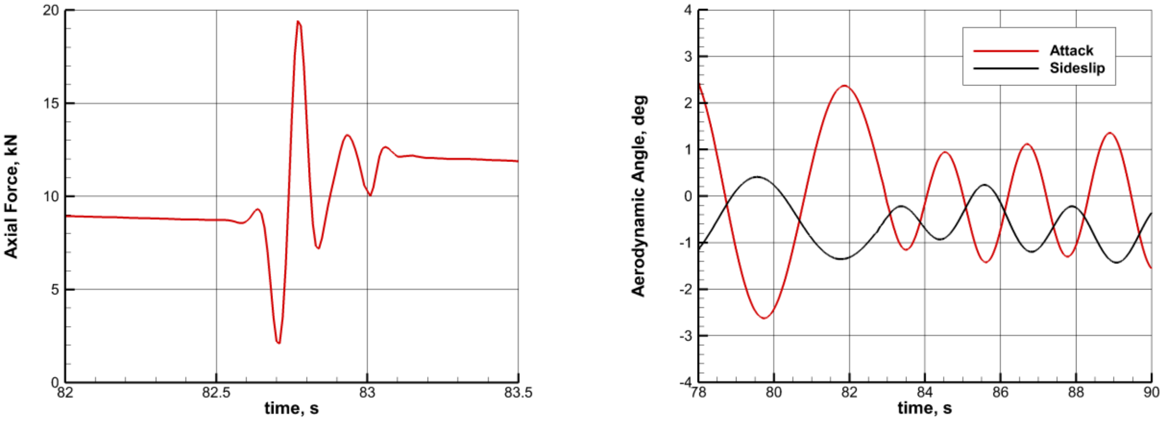

(a) (b)

Figure 20. a) Axial force during SIAD inflation, and b) aerodynamic angle history showing increase in pitch frequency after SIAD inflation.

As shown in Fig. 21, activating the maximum strength inflation transient model in simulation changes the vehicle dynamics. From a qualitative point of view, the model appears to be conservative.

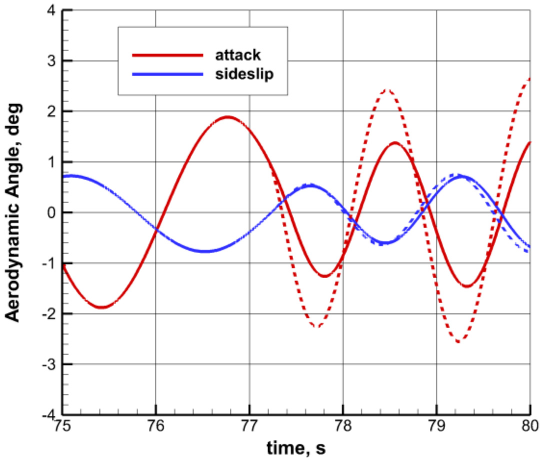

Figure 21. Inflation transient induced vehicle dynamics in simulation, denoted by dashed lines.

F. SIAD Cruise

The SIAD cruise phase began after full inflation at about *t*=83.1 s and ended at approximately *t*=161.3 s, just before PDD deployment. During this time, the Mach number decreased from 4.06 to 2.73, the dynamic pressure decreased from 317 to 151 Pa, then rose again to 422 Pa as the TV gained, then lost altitude. The TV total angle of attack ranged from less than 0.1° to 2.75° during cruise. As shown in Fig. 22(a), the reconstructed coefficient falls well within 3σ model uncertainties, and is correlated with freestream dynamic pressure as shown in Fig. 22(b).

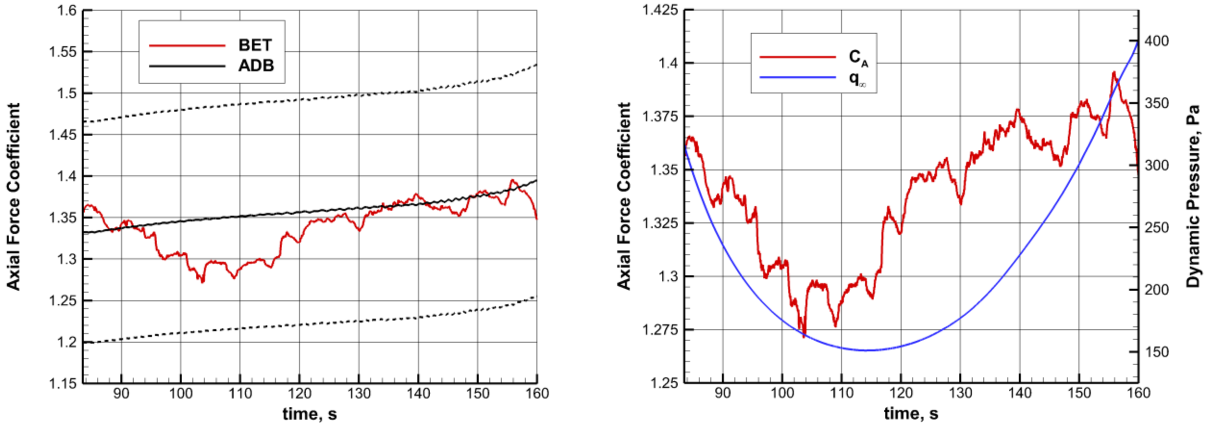

(a) (b)

Figure 22. SIAD cruise phase a) axial force coefficient, with 3σ model uncertainties denoted by dashed lines, and b) reconstructed axial force coefficient and freestream dynamic pressure.

Reconstructed pitching and yawing moment coefficients are compared against the model values in Fig. 22. The reconstructed amplitudes exceed those of the model, implying that the model moment curve slopes are shallow. Analysis showed that this was indeed the case, and a consequence of the model having inadequate resolution in the angle of attack dimension, with the first nonzero angle of attack point at 10°. The moment curve slope was changed by adding ADB data points at 2° angle of attack. A nonzero sideslip trim angle during the cruise phase is shown in Fig. 23, and could be caused by a radial *cg* offset of about 0.011 m along the –y axis.

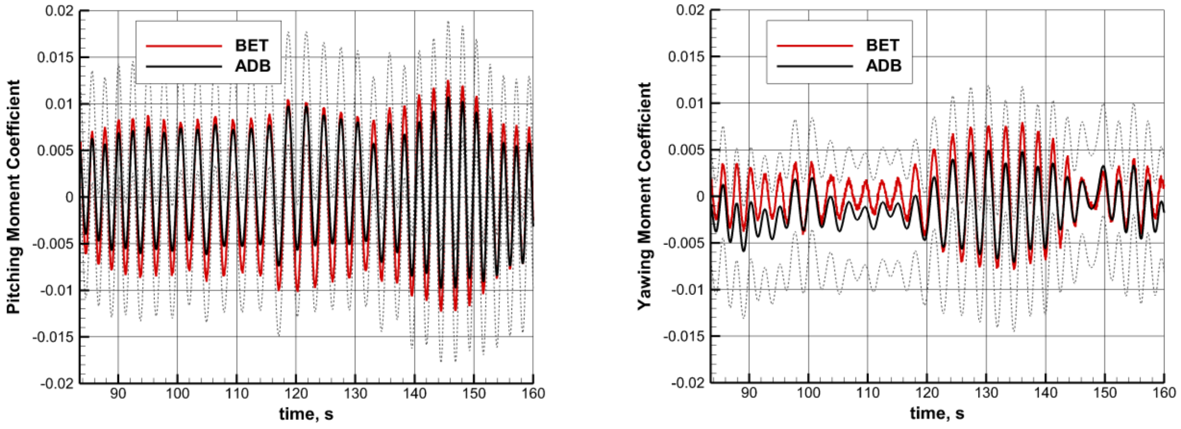

(a) (b)

Figure 23. a) Pitching moment coefficients, and b) yawing moment coefficients plotted against model values. Dashed lines denote model 3σ uncertainties.

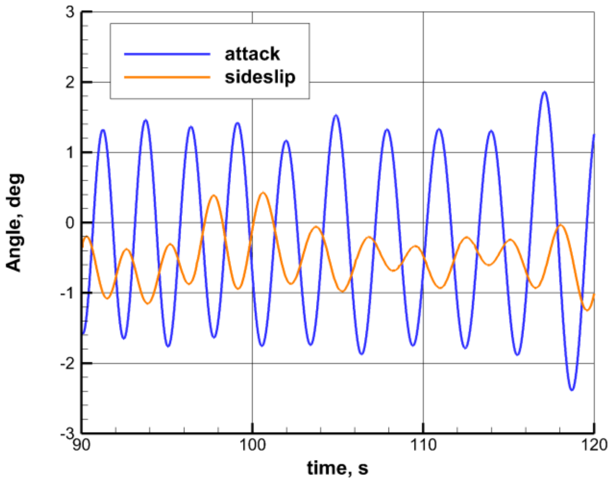

Figure 24. Sideslip trim angle of approximately 0.5° during SIAD cruise.

As detailed in Ref. 31, the mean pitch damping coefficient during SIAD cruise was estimated for a 10 s portion of the trajectory using a method based on the Euler-Cauchy (EC) equation[36]. The trajectory segment about the apex was used, as constant density is a limiting assumption of the EC method. As shown in Fig. 24(a), an analytical solution to the EC equation was fit to the reconstructed pitch rate data. The pitch damping coefficient extracted from each time step are plotted in Fig. 24(b) with the ADB model pitch damping curves. The data indicate that the SIAD had greater dynamic stability than predicted, and no significant dynamic instability was evidenced.

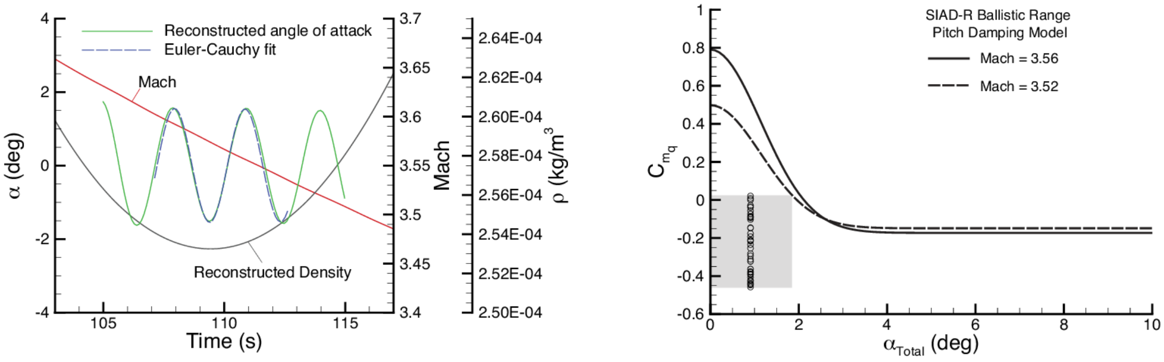

(a) (b)

Figure 25. a) Curve fit to reconstructed oscillation, Mach number, and density, and b) extracted C_{mq} points plotted with pitch damping model. From Ref. 31.

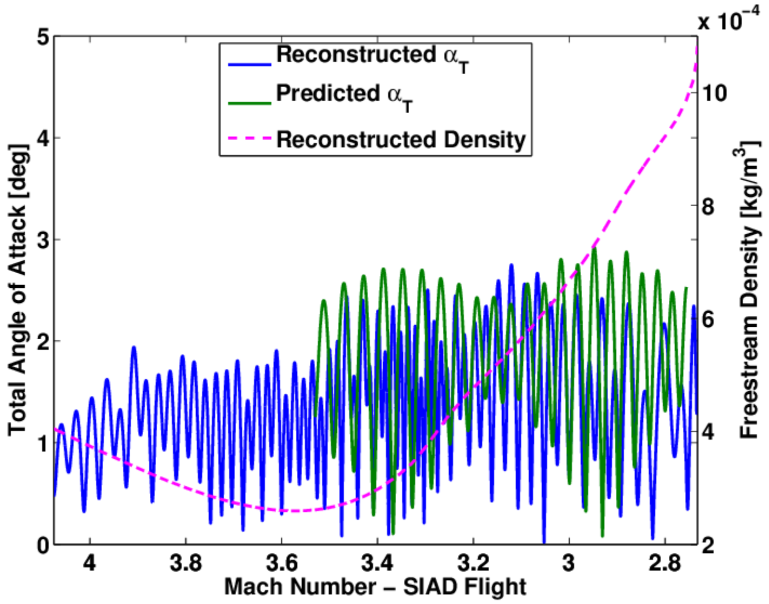

Figure 26. Reconstructed and predicted total angle of attack during SIAD cruise. From Ref. 31.

V. Aerodynamic Model Changes

Since SFDT-1 targeting, the aerodatabase has been updated with model changes to the spin, despin, powered phase, and SIAD cruise aerodynamic models. The spin and despin models were updated prior to flight but were not used in targeting activity due to time constraints. Updates to the powered phase and SIAD cruise models were motivated by comparisons to the reconstructed flight data.

Spin and despin model updates utilized the most accurate flight article geometry available, which had been changed to include plume deflectors, TPS, bridle covers, and other modifications. Additionally, spin-up freestream conditions and angle of attack were updated to reflect those expected after drop. In post-flight simulations of SFDT-1, the updated spin-up model yielded pitch and yaw time histories in much better agreement with reconstruction than the previous model, however its use also led to 1.5 km peak altitude loss.

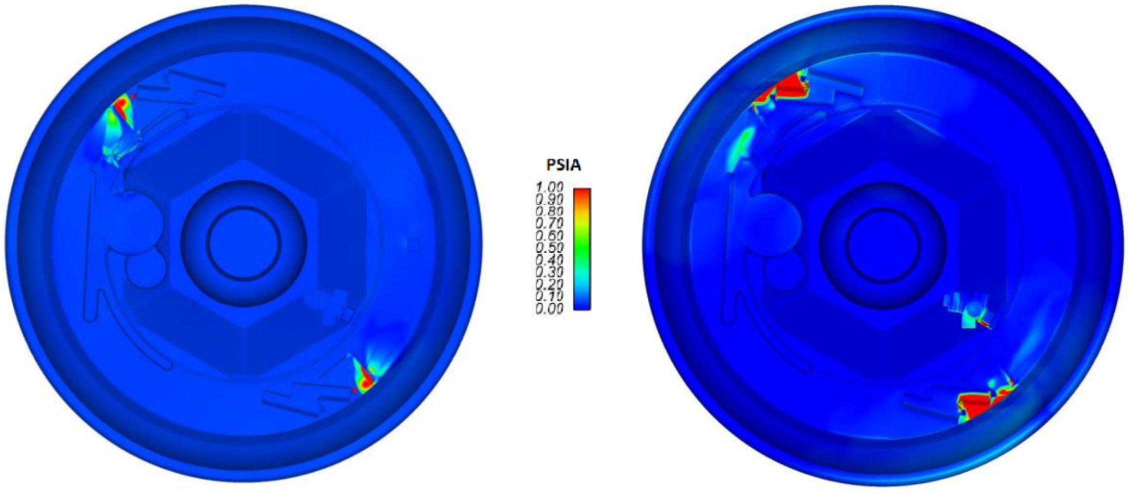

(a) (b)

Figure 27. Updated model computed aftbody pressure contours for spin motors 1&3 (a) and 2&4 (b).

As mentioned previously, the SFDT-1 reconstruction showed that the powered phase moment coefficient was overpredicted in the sub- and transonic regime, leading to underpredicted peak altitude in simulation. To better understand the cause of the model inaccuracy, CFD was run with high-fidelity TV geometry using the Loci-CHEM code at sub- and transonic conditions, both with and without the STAR-48 plume. The powered case moment coefficients largely agreed with flight reconstruction, implying that the sub- and transonic powered phase aerodynamics are sensitive to the TV base geometry. The results also suggested that the powered phase axial force was overpredicted, however the integrated effect of the drag error was deemed insignificant. A correction to the ADB was implemented to reduce the powered phase moment coefficient magnitude in the sub- and transonic regime, and increases simulated peak altitude by 2.66 km. The pre-flight model, reconstruction, and post-flight model are compared in Fig. 27(b). When the new model is combined with other post-flight changes to models outside the ADB, the loft of SFDT-1 is recreated in flight simulations.

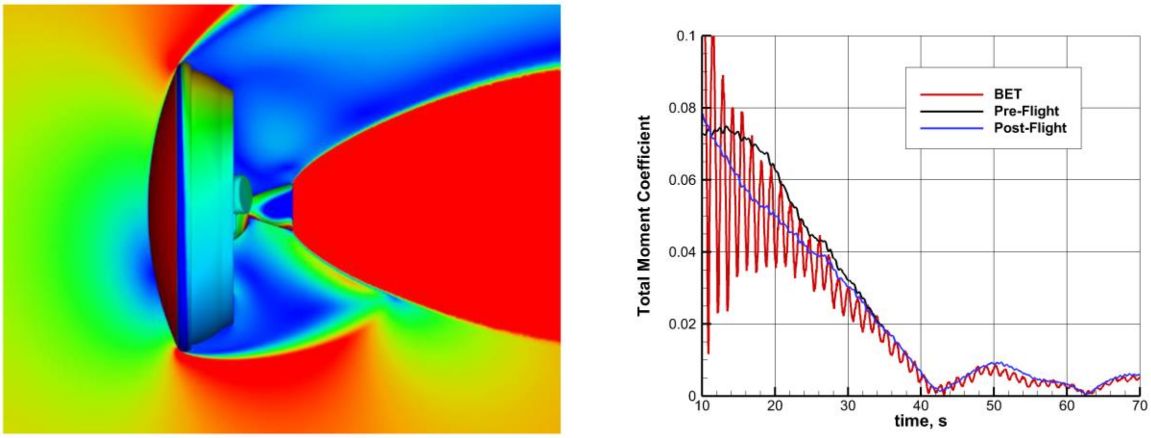

(a) (b)

Figure 28. a) Loci-CHEM subsonic powered phase solution; b) comparison of pre-flight, reconstructed, and post-flight powered phase total moment coefficient.

The SFDT-1 reconstruction indicated that the predicted SIAD-R cruise phase pitching moment slope was shallow. This was found to be due to insufficient angle of attack resolution in the ADB, where the first nonzero point was at 10°. Cases for each Mach number were run at 2° angle of attack, which increased the pitching moment slope by 15.6%.

VI. Conclusion

Prior to flight, the Low Density Supersonic Decelerator (LDSD) Supersonic Flight Dynamics Test (SFDT-1) was simulated extensively in order to support vehicle development, conduct trade studies, and to target, evaluate, and optimize flight system performance. Aerodynamic models for the SFDT-1 test vehicle (TV) are integrated within flight simulations with a routine referred to as the aerodatabase (ADB). The ADB contains aerodynamic models for all phases of TV flight: drop, spin-up, powered ascent, coast, despin, SIAD inflation, and SIAD cruise. Each model is implemented with tables of aerodynamic coefficients, aerodynamic uncertainties, model equations, and supporting subroutines which link the flight phases together. The TV aerodynamic models were constructed from computational and experimental data sources, where static aerodynamics were predicted with computational fluid dynamics (CFD), and dynamic derivatives were obtained from ballistic range tests.

While SFDT-1 was largely successful, its trajectory was off-nominal, lofting to nearly 8.5 km higher than predicted. Flight aerodynamics reconstructed with the NewSTEP code showed that an overpredicted powered phase pitch stability was a significant aerodynamic contributor to lofting. Reconstructed flight data and CFD analysis were used to adjust the powered phase model to match trajectory lofting in simulation. SIAD and coast phase aerodynamic models predicted flight aerodynamics well within uncertainties. Spin, despin, and SIAD inflation models could not be assessed directly from reconstructed aerodynamics due to numerical oscillations in the reconstructed solution.

Acknowledgments

The authors are thankful of the work of SFDT-1 flight mechanics and flight reconstruction team members at NASA Langley Research Center and Jet Propulsion Laboratory, including Eric Blood, Angela Bowes, Som Dutta, Jason Ginn, Mark Ivanov, Chris Karlgaard, Prasad Kutty, Clara O'Farrell, Dick Powell, Eric Queen, Bill Strauss, Scott Striepe, and Joseph White.

References

[1] Edquist, K.T., Korzun, A.M., Dyakonov, A.A., Studak, J.W., Kipp, D.M., and Dupzyk, I.C., "Development of Supersonic Retropropulsion for Future Mars Entry, Descent, and Landing Systems," Journal of Spacecraft and Rockets, Vol. 51, No. 3, May-June 2014.

[2] Hughes, S.J., Cheatwood, F.M., Dillman, R.A., Wright, H.S., DelCorso, J.A., and Calomino, A.M., "Hypersonic Inflatable Aerodynamic Decelerator (HIAD) Technology Development Overview," 21st AIAA Aerodynamic Decelerator Systems Technology Conference and Seminar, May 2011, Dublin.

[3] Clark, I.G., Adler, M., and Rivellini, T.P., "Development and Testing of a New Family of Supersonic Decelerators," AIAA Paper 2013-1252.

[4] Striepe, S.A., Powell, R.W., Desai, P.N., Queen, E.M., Way, D.W., Prince, J.L., Cianciolo, A.M., Davis, J.L., Litton, D.K., Maddock, R.M., Shidner, J.D., Winski, R.G., O'Keefe, S.A., Bowes, A.G., Aguirre, J.T., Garrison, C.A., Hoffman, J.A., Olds, A.D., Dutta, S., Zumwalt, C.H., White, J.P., Brauer, G.L., Marsh, S.M., "Program To Optimize Simulated Trajectories II (POST2): Utilization Manual," Vol. II, Version 3.0.NESC, 2014

[5] Balaram, J., Austin, R., Banerjee, P., Bentley, T., Henriquez, D., Martin, B., McMahon, E., and Sohl, G., "DSENDS - A High-Fidelity Dynamics and Spacecraft Simulator for Entry, Descent and Surface Landing," IEEE 2002 Aerospace Conference, Big Sky, Montana, March 9-16, 2002.

[6] Timmons, J.D., "Viking Balloon Launched Decelerator Test," 27th Congress International Astronautical Federation, Anaheim, October 1976.

[7] Moog, R.D., Bendura, R.J., Timmons, J.D., and Lau, R.A., "Qualification Flight Tests of the Viking Decelerator System," AIAA Paper 73-457, May 1973.

[8] B.T. Cook, G. Blando, A. Kennett, M. Von Der Heydt, J.L. Wolff, and M. Yerdon, "High Altitude Supersonic Decelerator Test Vehicle," AIAA Aerodynamic Declerator Systems Conference, March 2013, Daytona.

[9] Clark, I.G., Adler, M., and Rivellini, T.P., "Development and Testing of a New Family of Supersonic Decelerators," AIAA Paper 2013-1252.

[10] Gnoffo, P.A., Weilmuenster, J., Braun, R.D., and Cruz, C.I., "Influence of Sonic Line Transition on Mars Pathfinder Probe Aerothermodynamics," Journal of Spacecraft and Rockets, Vol. 33, No. 2, March-April 1996, pp. 169-177.

[11] http://fun3d.larc.nasa.gov

[12] Nichols, R.H., and Buning, P.G., "User's Manual for OVERFLOW 2.2," Version 2.2, August 2010.

[13] Wright, M.J., White, T.R., and Mangini, N., "Data Parallel Line Relaxation (DPLR) Code User Manual: Acadia, Version 4.01.1," NASA TM 2009-215388, 2009.

[14] Luke, E. A., Tong, X-L., Wu, J., Tang, L., and Cinnella, P., "CHEM: A Chemically Reacting Flow Solver for Generalized Grids," AIAA 2003.

[15] Yates, L., "Aerodynamic Coefficients from Aeroballistic Range Testing of Deployed and Stowed-SIAD SFDT Models," Final Report, May 22, 2012.

[16] Schoenenberger, M., Dyakonov, A., and Van Norman, J., "Mars Science Laboratory Aerodynamic Database Release 1.0," NASA Langley Research Center, May 2012.

[17] Samareh, J., "GridTool: A Surface Modeling and Grid Generation Tool," Proceedings of the Workshop on Surface Modeling, Grid Generation, and Related Issues in CFD Solutions, NASA CP-3291, May 9-11, 1995.

[18] Pirzadeh, S., "Viscous Unstructured Three-Dimensional Grids by the Advancing-Layers Method," AIAA 94-0417, January 1994.

[19] Schoenenberger, M., Van Norman, J., Rhode, M., and Paulson, J., "Characterization of Aerodynamic Interactions with the Mars Science Laboratory Reaction Control System Using Computation and Experiment," 51st AIAA Aerospace Sciences Meeting, Grapevine, January 2013.

[20] Dyakonov, A.A., Glass, C.E., Desai, P.N., and Van Norman, J.W., "Analysis of Effectiveness of Phoenix Entry Reaction Control System," Journal of Spacecraft and Rockets, Vol. 48, No. 5, September-October 2011.

[21] Smith, S.D., "High Altitude Supersonic Flow of Chemically Reacting Gas-Particle Mixtures – Volume 1 – A Theoretical Analysis and Development of the Numerical Solution," LMSC HREC TM D390409, Lockheed Missiles & Space Company, Huntsville, AL, October 1974.

[22] Evans, R.M., "Boundary Layer Integral Matrix Procedure BLIMPJ User's Manual," UN-75-64 Aerotherm, Mountain View, CA, July 1975.

[23] Marcum, D.L., "Adaptive Unstructured Grid Generation for Viscous Flow Applications," AIAA Journal, Vol. 34, No. 11, p. 2440, 1996.

[24] Alliant Techsystems, Inc., "ATK Space Propulsion Products Catalog," August 2012.

[25] CAP Aerodynamics, "Orion Aerodynamics Databook Version 0.53," NASA CXP-72167, May 2009.

[26] Roberts, B.B., Wallace, R.O., Craig, M.K, and Kanipe, D.B., "Rocket Exhaust Plume Induced Flowfield Interaction Experiences with the Space Shuttle," AIAA 18th Thermophysics Conference, Montreal, 1983.

[27] Bohon, H.L. and Miserentino, R., "Deployment and Performance Characteristics of 5-Foot-Diameter Attached Inflatable Decelerators From Mach Number 2.2 to 4.4," NASA TN D-5840, August 1970.

[28] Giersch, L., Rivellini, T., Clark, I., Shook, L., Ware, J., and Welch, J., "SIAD-R: A Supersonic Inflatable Decelerator for Robotic Missions to Mars," AIAA Aerodynamic Decelerator Systems Conference, Daytona, March 2013.

[29] Muppidi, S., Tang, C., Van Norman, J.W., Bose, D., Clark, I., and Coatta, D., "Aerodynamic Analysis of Next Generation Supersonic Decelerators," 32nd AIAA Applied Aerodynamics Conference, Atlanta, June 2014.

[30] Tang, C., Muppidi, S., Van Norman, J.W., Tanimoto, R., Bose, D., and Clark, I., "Aerodynamic and Aerothermal Analysis of the Supersonic Inflatable Aerodynamic Decelerator-Robotic (SIAD-R)," 23rd AIAA Aerodynamic Decelerator Systems Technology Conference and Seminar, Daytona, March-April 2015.

[31] Kutty, P., Karlgaard, C.D., Blood, E.M., O'Farrell, C., Ginn, J.M., Schoenenberger, M., and Dutta, S., "Supersonic Flight Dynamics Test: Trajectory, Atmosphere, and Aerodynamics Reconstruction," AAS 15-224.

[32] Karlgaard, C.D., Tartabini, P.V., Blanchard, R.C., Kirsch, M., and Toniolo, M.D., "Hyper-X Post-Flight Trajectory Reconstruction," Journal of Spacecraft and Rockets, Vol. 43, No. 1, 2006, pp. 105-115.

[33] Karlgaard, C.D., Beck, R.E., Derry, S.D., Brandon, J.M., Starr, B.R., Tartabini, P.V., and Olds, A.D., "Ares I-X Trajectory Reconstruction: Methodology and Results," Journal of Spacecraft and Rockets, Vol. 50, No. 3, 2013, pp. 641–661.

[34] Schoenenberger, M., Van Norman, J., Karlgaard, C.D., Kutty, P., and Way, D., "Assessment of the Reconstructed Aerodynamics of the Mars Science Laboratory Entry Vehicle," Journal of Spacecraft and Rockets, Vol. 51, No. 4, 2014, pp. 1076-1093.

[35] Dutta, S., Bowes, A.L., Striepe, S.A., Davis, J.L., Queen, E.M., Blood, E.M., and Ivanov, M.C., "Supersonic Flight Dynamics Test 1 – Post-Flight Assessment of Simulation Performance," 25th AAS/AIAA Space Flight Mechanics Meeting, Willaimsburg, Virginia, January-February 2015.

[36] Schoenenberger, M., Queen, E. M., and Litton, D., "Oscillation Amplitude Growth for a Decelerating Object with Constant Pitch Damping," AIAA 2006–6148, 2006.